JOURNAL OF COMPUTATIONAL PHYSICS **129,** 245–262 (1996)
ARTICLE NO. 0248

Designing an Efficient Solution Strategy for Fluid Flows

1. A Stable High Order Finite Difference Scheme and Sharp Shock Resolution for the Euler Equations*

Margot Gerritsen and Pelle Olsson

SCCM Program, Gates Building 2B, M/C 9025, Stanford University, Stanford, California 94305
E-mail: margot@sccm.stanford.edu; olsson@sccm.stanford.edu

Received February 5, 1996; revised July 23, 1996

We derive high-order finite difference schemes for the compressible Euler (and Navier–Stokes equations) that satisfy a semidiscrete energy estimate and present an efficient strategy for the treatment of discontinuities that leads to sharp shock resolution. The formulation of the semidiscrete energy estimate is based on symmetrization of the equations, a canonical splitting of the flux derivative vector, and the use of difference operators that satisfy a discrete analogue to the integration-by-parts procedure used in the continuous energy estimate. For the Euler equations, the symmetrization is designed such as to preserve the homogeneity of the flux vectors. Around discontinuities or sharp gradients, refined grids are created on which the discrete equations are solved after adding artificial viscosity. The positioning of the subgrids and computation of the viscosity are aided by a detection algorithm which is based on a multiscale wavelet analysis of the pressure grid function. The wavelet theory provides easy-to-implement mathematical criteria to detect discontinuities, sharp gradients, and spurious oscillations quickly and efficiently. As the detection algorithm does not depend on the numerical method used, it is of general interest. The numerical method described and the detection algorithm are part of a general solution strategy for fluid flows, which is currently being developed by the authors and collaborators.

1. INTRODUCTION

In this paper we present the numerical method that underlies a new, general solution strategy for solving flows governed by the compressible Euler or Navier–Stokes equations and discuss a novel approach for the treatment of discontinuities that leads to sharp shock resolution. The solution strategy that we are suggesting and developing is designed particularly for flows that are smooth in large parts of the domain and process distinct regions in which the flow changes rapidly, e.g., in the presence of shocks, or in which the flow needs to be resolved accurately, e.g., in the presence of interesting small scale phenomena. There is a plethora of problems in computational fluid dynamics that have these characteristics. Examples are the numerical simulation of flow over an airfoil at high Mach number, or oceanographic and atmospheric problems with unstable wavefronts. The emphasis in the design of the solution strategy is on simplicity and efficiency, both in computational time and memory consumption. It is based on

- stable, high-order finite difference schemes with central discretization
- local grid adaptation in areas where:
  - —estimated numerical errors grow too large
  - —small scale phenomena need to be resolved accurately
  - —shocks are present
- Addition of an artificial viscosity term in refined shock regions
- Composite (overlapping) grids to handle complicated multidimensional flow domains.

Here, we derive the finite difference scheme, artificial viscosity and construct a detection algorithm that aids the local grid adaptation. We show results on test problems in one dimension. The difference scheme and detection algorithm can be extended to multiple dimensions in a straightforward way. Error estimations, composite grid methods, and multidimensional test problems will be discussed in forthcoming reports.

The high order of accuracy of the numerical method allows for the use of coarse grids in regions where the flow is slowly varying. In multidimensional applications this reduces both computational costs and memory requirements significantly. Finite difference methods with central discretization require very little memory and are easy to parallelize. In the past, it was not known how to construct boundary difference operators of sufficient

* This work has been sponsored by NSF Grant ASC 9318166-002 and by NASA under Contract NAS 2-13721.

0021-9991/96 $18.00

accuracy that lead to (strict) stability. But recently, Kreiss, Scherer, and Olsson [11, 21] developed a technique to design strictly stable high order finite difference schemes for linear problems based on the energy method. Olsson showed that extension of the energy method to nonlinear systems is possible [20]. He employs a splitting of the flux derivative vector after symmetrization of the system. To facilitate the derivation of the energy estimates for the Euler equations, the variable transformation should preserve the homogeneity of the flux vector. We show that these conditions can be met for a specific class of transformations. For the compressible Navier–Stokes equations this condition is not necessary and a larger class of transformations can be used. The obtained energy estimates, or entropy inequalities, imply that the (semi-)discrete solutions possess stability properties akin to those of the exact solutions of the governing equations, namely the second law of thermodynamics. These results were previously obtained for finite element methods by Hughes, Franca, and Mallet in [8].

Inspired by the stability results we devise a high-order scheme using the aforementioned transformation and splitting of the flux derivative vector. It results in a system of ordinary differential equations that is solved using a TVD Runge–Kutta time integration. We refer to it as the split high-order entropy-conserving (SHOEC) scheme which forms the backbone of our solution strategy. In this paper it is formulated in one space dimension but the results generalize to the multidimensional case.

The stability properties of the SHOEC scheme allow for the formulation of local error estimates based on linearization of the equations. This can be used in a grid adaptation procedure in which the grid is refined locally if the estimated errors grow beyond a certain threshold (see, for example, [29]). But there are situations in which local grid refinement is required that cannot be detected by error estimation. Here, we focus on the presence of shocks. High order central discretizations are notorious for introducing spurious oscillations at discontinuities. We solve this problem by introducing (a sequence of) refined grids close to the shock on which the equations are supplemented by an artificial viscosity term. We use a scalar artificial viscosity term that does not destroy the stability results and supports near one-point shocks for stationary shocks. For moving shock and very strong stationary shocks, the artificial viscosity can be chosen large enough to damp all oscillations at the finest grid while preserving sharp resolution at the coarser levels. We remark that the artificial viscosity term can be chosen as large as desired if the fine grid is confined to the shock region and if the grid size of the fine grid is sufficiently small. We also refer to a recent result by Sjögreen [26] that the accuracy of any numerical method reduces to first order at a shock in the systems case. Local grid refinement is therefore highly desirable.

This strategy is effective if the shock location can be detected accurately. For this purpose, we developed an efficient algorithm that can also be used for the detection of fronts and interfaces. Since it does not depend on the numerical method used in the computations it is of general interest. The detection algorithm is based on a multiscale wavelet analysis of the pressure grid function. It is derived from a noise-detection algorithm developed by Mallat and coworkers [16, 17] in signal analysis. Most existing shock detection algorithms search for maxima in the first or points of inflection of the grid functions. The derivatives are evaluated numerically at the scale of the grid. At this scale it is hard to distinguish between maxima that belong to spurious oscillations and those that correspond to shocks. Besides, it is difficult to extract information about the shock states when the discrete data are distorted by oscillations. If, instead, the grid function is analyzed on both the scale of the grid and a sequence of larger scales, these problems are resolved; the behavior at the larger scales is determined by phenomena such as shocks or sharp gradients, while local oscillations only influence the smaller scales. The number of available scales is limited because we work in a discrete and finite domain. The question is how to construct a reliable algorithm to determine the local behavior of the grid function based on this limited information. The *wavelet* theory supplies the answers. In a multiscale wavelet analysis a function is convoluted with a family of wavelets, each varying in position and representing a different scale or frequency. For a special class of families a direct correlation exists between the local regularity of the function and the behavior of small, easy-to-determine, sets of wavelet coefficients. Moreover, they allow the formulation of a fast wavelet transform which leads to an efficient detection algorithm. The underlying wavelet theory is presented and the choice of the wavelet family is motivated. We thereby focus on issues that are relevant in the context of computational fluid dynamics.

The sharp shock resolution and the computational efficiency of the above-described SHOEC scheme with local grid adaptation are illustrated by numerical experiments for the one-dimensional Euler equations. We compare our results to those obtained with a high order ENO scheme as constructed by Lindström [14]. Both shock detection and artificial viscosity are generalizable to multiple space dimensions and are being implemented. We emphasize that the resulting scheme is a *shock-capturing* scheme as we do not require any a priori knowledge of the shock location.

We start the paper by deriving the SHOEC scheme in Section 2 for the Euler and Navier–Stokes equations. In Section 3 the matrix and scalar viscosity are constructed. We give relevant wavelet theory, devise the shock detection algorithm, and discuss specific implementation issues related to the Euler equations in Section

4. In the final two sections we present results and conclusions.

2. DERIVING THE SHOEC SCHEME

To illustrate the concepts that lead to the derivation of the SHOEC scheme, we consider the one-dimensional Euler equations written as a system of conservation laws

$$\begin{aligned} &u_t + f_x = 0, \quad u, f \in \mathbb{R}^d, \quad x \in (x_0, x_1), \quad t > 0, \\ &u(x, 0) = \phi(x). \end{aligned} \tag{2.1}$$

The state vector u and flux vector f are given by

$$u = \begin{bmatrix} \rho \\ \rho v \\ E \end{bmatrix}, \quad f = \begin{bmatrix} \rho v \\ \rho v^2 + p \\ v(E + p) \end{bmatrix}. \tag{2.2}$$

The variables v and p are the velocity and pressure of the gas. The latter is related to u through the equation of state for a polytropic gas

$$p = (\gamma - 1)(E - \tfrac{1}{2}\rho v^2), \tag{2.3}$$

where $\gamma = 1.4$ is the ratio of specific heats c_p/c_v. At the boundaries $x = x_0$ and $x = x_1$ of the domain we prescribe data for the in-going characteristic variables ω_I by

$$\omega_I(x_i, t) = \psi_i(t), \quad i = 0, 1. \tag{2.4}$$

The flux vector $f(u)$ is a homogeneous function of order one, i.e., $f(\theta u) = \theta f(u)$. The Jacobian f_u is nonsymmetric.

The entropy S is given by

$$S = c_v \log(p\rho^{-\gamma}) + \text{const.}$$

In the remainder of this paper we will use a simplified scaled expression for the entropy of the form

$$S = \log(p\rho^{-\gamma}). \tag{2.5}$$

2.1. *Continuous Energy Estimates*

Stability can be ensured by the energy method. As explained in [20], a continuous energy estimate can be derived for (2.1) if it is written in symmetrized form using a variable transformation $w = w(u)$. In the transformed system

$$u_t + f(u)_x = u_t + \tilde{f}(w(u))_x = u_w w_t + \tilde{f}_w w_x = 0, \tag{2.6}$$

the Jacobian $\tilde{f}_w$ is symmetric, and u_w is symmetric and positive definite. The key to establishing an energy estimate lies in a special splitting of the flux derivative vector $\tilde{f}_x$ and u_t referred to as the *canonical splitting*. We choose w such that both $\tilde{f}(w)$ and $u(w)$ are homogeneous functions of w, i.e.,

$$\begin{aligned} u(\theta w) &= \theta^\beta u(w), \\ \tilde{f}(\theta w) &= \theta^\beta \tilde{f}(w), \quad \theta, \beta \in \mathbb{R}. \end{aligned} \tag{2.7}$$

They satisfy Euler's differential equation

$$\begin{aligned} \tilde{f}_w w &= \beta \tilde{f} \\ u_w w &= \beta u. \end{aligned} \tag{2.8}$$

Then, the canonical splitting results in

$$\begin{aligned} f_x &= \frac{1}{\beta + 1}(\tilde{f}_w w)_x + \frac{1}{\beta + 1}\tilde{f}_w w_x \\ &= \frac{\beta}{\beta + 1}\tilde{f}_x + \frac{1}{\beta + 1}\tilde{f}_w w_x, \quad \beta \neq -1. \end{aligned} \tag{2.9}$$

Similarly we obtain

$$u_t = \frac{\beta}{\beta + 1} u_t + \frac{1}{\beta + 1} u_w w_t. \tag{2.10}$$

Using the above splittings in (2.1) and taking the inner product with w gives

$$\begin{aligned} &\frac{\beta}{\beta + 1}(w, u_t) + \frac{1}{\beta + 1}(w, u_w w_t) \\ &\quad = -\frac{\beta}{\beta + 1}(w, \tilde{f}_x) - \frac{1}{\beta + 1}(w, \tilde{f}_w w_x). \end{aligned} \tag{2.11}$$

Integration by parts and the homogeneity relations (2.8) yield

$$\begin{aligned} \frac{d}{dt}\|w\|_u^2 &\equiv \frac{d}{dt}(w, u_w w) \\ &= (w_x, \tilde{f}_w w) - (w, \tilde{f}_w w_x) - w^{\mathrm{T}} \tilde{f}_w w \big|_{x_0}^{x_1}. \end{aligned} \tag{2.12}$$

The symmetry of $\tilde{f}_w$ leads to the relation

$$\frac{d}{dt}\|w\|_u^2 = -w^{\mathrm{T}} \tilde{f}_w w \big|_{x_0}^{x_1}, \tag{2.13}$$

which is independent of β.

Now, the following estimate can be shown [20]

$$\frac{d}{dt}\|w\|_u^2 \le \psi_0^{\mathrm{T}}\,\Lambda_I(w(x_0,t))\psi_0 + \psi_1^{\mathrm{T}}\Lambda_I(w(x_1,t))\psi_1,$$

where $\Lambda_I(w(x_i,\ t))$ are the absolute eigenvalues corresponding to the in-going characteristic variables at the boundary in question. As u_w and Λ_I both depend on w this is not an energy estimate in the usual sense. But as they are both positive definite we will refer to the inequality as a *generalized energy estimate.* Below, we will see that it is in fact an entropy inequality.

2.2. *Symmetrization*

Harten [6] derived a family of symmetric transformations $w = \eta_u$, where $\eta(u)$ is a scalar and convex function given by $\eta(u) = \rho h(S)$. The relation between entropy functions and symmetrizing variables was found by Mock [19]. The function $h(S)$ is an arbitrary but differentiable function of the entropy S given by (2.5). The variables w are referred to as the entropy variables. The relation $w = \eta_u$ gives

$$w = \frac{(\gamma-1)\dot{h}}{p}\quad\left[E + \frac{p}{\gamma-1}(h/\dot{h} - (\gamma+1))\quad -\rho v\quad \rho\right]^{\mathrm{T}},$$
$$\dot{h} \equiv \frac{dh}{dS}, \tag{2.14}$$

from which it easily follows that

$$u = \frac{p}{(\gamma-1)\dot{h}}[w_3\quad -w_2\quad w_1 - \dot{h}(h/\dot{h} - (\gamma+1))]^{\mathrm{T}}. \tag{2.15}$$

The homogeneity requirement of $\tilde{f}(w)$ and $u(w)$ restricts the choice of entropy functions. Equation (2.15) shows that $u(w)$ is homogeneous provided the terms $h/\dot{h}$ and $(\gamma+1)$ in the expression for $u_1 = \rho$ have the same dimension. Otherwise it is not possible to extract a common power of θ. Thus, $\dot{h}/h \equiv \kappa$, where κ is a constant, and consequently

$$h(S) = Ke^{\kappa S} = K(p\rho^{-\gamma})^{\kappa},\quad K,\kappa \neq 0. \tag{2.16}$$

This exponential family leads to a homogeneous function $u(w)$ that satisfies $u(\theta w) = 1/\theta^{(1-\gamma)\kappa}\,u(w)$. Function $h(S)$ of the form (2.16) were also discussed by Harten [6]. Using his notation we choose $\kappa \equiv 1/(\alpha+\gamma)$, $\alpha \in \mathbb{R}$. It follows that $\beta = (\alpha+\gamma)/(1-\gamma)$. The flux $\tilde{f}(w)$ has the same homogeneity constant.

Now, (2.14) and (2.15) yield the simple expressions

$$w = \frac{p^*}{p}\left[u_3 + \frac{\alpha-1}{\gamma-1}p\quad -u_2\quad u_1\right]^{\mathrm{T}}, \tag{2.17}$$

$$u = \frac{p}{p^*}\left[w_3\quad -w_2\quad w_1 - \frac{\alpha-1}{\gamma-1}p^*\right]^{\mathrm{T}}, \tag{2.18}$$

where

$$p^* = \chi e^{S/(\alpha+\gamma)} = \chi(p\rho^{-\gamma})^{1/(\alpha+\gamma)},$$
$$p = \chi^{-\beta}((p^*)^{\alpha}w_3^{\gamma})^{1/(1-\gamma)}, \tag{2.19}$$

with $\chi = -K/\beta$. The variable p^* satisfies an equation similar to the equation of state (2.3)

$$p^* = \frac{(\gamma-1)}{\alpha}\left(w_1 - \frac{1}{2}\frac{w_2^2}{w_3}\right). \tag{2.20}$$

The homogeneity of $\tilde{f}(w)$ follows from Eqs. (2.19), (2.20), and (A.1). The convexity condition on the entropy function given by $\eta = \rho h(S)$ leads to the conditions $\chi < 0$ and $\alpha > 0$ or $\alpha < -\gamma$. This excludes the unacceptable case $\beta = -1$. We note that for $\alpha = 1$ and $\alpha = (1-2\gamma)$ the expressions for p^*/p and p/p^* simplify: for $\alpha = 1$ we get $p^*/p = \chi(p\rho)^{-7/12}$ and $p/p^* = \chi^6(p^*w_3)^{-7/2}$; for $\alpha = (1-2\gamma)$ we have $p^*/p = \chi(p/\rho)^{-7/2}$ and $p/p^* = \chi^{-1}(p^*/w_3)^{7/2}$.

Equation (2.17) and the homogeneity property $u_w w = \beta u$ give

$$\|w\|_u^2 = \beta\int_{x_0}^{x_1} w^{\mathrm{T}}u\,dx = (\beta+1)\int_{x_0}^{x_1} K\rho\,e^{\kappa S}\,dx$$
$$= (\beta+1)\int_{x_0}^{x_1}\eta\,dx. \tag{2.21}$$

The right-hand side of (2.12) can be shown to be equal to $-(\beta+1)\,q|_{x_0}^{x_1}$, where q is the entropy flux (see [6]) corresponding to the entropy function η. Therefore we get

$$\frac{d}{dt}\int_{x_0}^{x_1}\eta\,dx = -q|_{x_0}^{x_1}. \tag{2.22}$$

As shown in [4], this enables the formulation of an entropy inequality, provided artificial viscosity is added to the scheme in flows with discontinuities.

A similar procedure can be applied to the compressible Navier–Stokes equations, i.e., symmetrization followed by the canonical splitting and the application of the energy method. As shown in [6] the viscous terms in the Navier–Stokes equations will be symmetric and positive definite after symmetrization for any member $\eta = \rho h(S)$ in Harten's family of generalized entropy functions. Hughes,

Franca, and Mallet showed in [8] that the heat flux term, if present, will only remain symmetric for $\eta = -\rho S$. This symmetry is needed in the derivation of the energy estimate. For this entropy function the flux vector and state vector are not homogeneous in the entropy variables w, but because of the different character of the boundary conditions (no-slip) the homogeneity properties are not required. The complete derivation of the generalized energy estimate for compressible Navier–Stokes is given in [4]. Here, the corresponding entropy inequality in fact represents the second law of thermodynamics. Using the discrete analogue to the energy estimate discussed below, this stability property is automatically inherited by the semidiscrete solution. In [4] the above derivations are also generalized to multiple space dimensions.

2.3. *Discretization*

When discretizing the Euler equations we apply the canonical splitting only to the spatial variables to retain a system of ordinary differential equations (ODEs). Using (2.9) the resulting semidiscrete equations are

$$\boldsymbol{u}_t = -\frac{\beta}{\beta+1} D\tilde{\boldsymbol{f}} - \frac{1}{\beta+1}\tilde{f}_w D\boldsymbol{w}, \quad \beta \neq -1. \tag{2.23}$$

We use bold notation to denote grid vectors like $\boldsymbol{u}^{\mathrm{T}} = (u_0^{\mathrm{T}}, u_1^{\mathrm{T}}, ..., u_n^{\mathrm{T}})$, where $u_i \in \mathbb{R}^d$, $i = 0, ..., n$. The difference operator D is defined below. Here, $\tilde{\boldsymbol{f}}_w$ denotes the block-diagonal matrix containing the Jacobians $\tilde{f}_w(w_j(u))$. In the remainder of this paper this convention is used for all matrices in vector equations.

It can be shown [22] that $\boldsymbol{u}$ will satisfy the analytic boundary conditions if the initial and boundary data satisfy suitable compatibility conditions. In much the same way as in the continuous case, we can derive a generalized energy estimate for the semidiscrete equations (2.23) for difference operators that satisfy a summation-by-parts principle (B.1) for Euler and Navier–Stokes in multidimensions [11, 27, 4]. Such difference operators are shown to exist for arbitrary, even order of accuracy. In the interior of the domain difference operators of order $2r$ take the form

$$D\boldsymbol{u} = D_0 R_{2r} \boldsymbol{u}, \tag{2.24}$$

where

$$\begin{aligned} R_{2r} &= \sum_{\nu=0}^{r-1} (-1)^\nu b_\nu (h^2 D_+ D_-)^\nu, \\ b_0 &= 1, \\ b_\nu &= \frac{\nu}{4\nu+2} b_{\nu-1}. \end{aligned} \tag{2.25}$$

D_0, D_+, and D_- are defined by

$$(D_0\boldsymbol{u})_j = \frac{1}{2h}(u_{j+1} - u_{j-1}), \quad (D_+\boldsymbol{u})_j = \frac{1}{h}(u_{j+1} - u_j),$$

$$(D_-\boldsymbol{u})_j = \frac{1}{h}(u_j - u_{j-1}),$$

where $h = x_{j+1} - x_j$ is the uniform mesh size. At the boundaries the difference operators are one-sided. The second- and fourth-order difference operators that are used in the computations are given in Appendix B. The second-order operator is second order in the interior and first order on the boundary, and the fourth-order operator is sixth order in the interior and third order on the boundary.

The equation (2.23) are solved in time by the total variation diminishing Runge–Kutta scheme formulated in [25]. For the system of ODEs $\boldsymbol{u}_t = L(\boldsymbol{u}(\boldsymbol{w}))$, it computes the solution $\boldsymbol{u}^{n+1}$ at the $(n+1)$th time step according to

$$\begin{aligned} \tilde{\boldsymbol{u}}_1 &= \boldsymbol{u}^n + \Delta t L(\boldsymbol{u}^n), \\ \tilde{\boldsymbol{u}}_2 &= 3/4\boldsymbol{u}^n + 1/4\tilde{\boldsymbol{u}}_1 + 1/4\Delta t L(\tilde{\boldsymbol{u}}_1), \\ \boldsymbol{u}^{n+1} &= 1/3\boldsymbol{u}^n + 2/3\tilde{\boldsymbol{u}}_2 + 2/3\Delta t L(\tilde{\boldsymbol{u}}_2), \end{aligned} \tag{2.26}$$

with time-step Δt and intermediate variables $\tilde{\boldsymbol{u}}_1$ and $\tilde{\boldsymbol{u}}_2$. Here,

$$L(\boldsymbol{u}(\boldsymbol{w})) \equiv -\frac{\beta}{\beta+1} D\tilde{\boldsymbol{f}} - \frac{1}{\beta+1}\tilde{f}_w D\boldsymbol{w}.$$

The Jacobian $\tilde{f}_w(w(u))$ is given in Appendix A. It has a simple form if expressed in the variables u. Its computation is therefore cheap, also taking into account its symmetry. The variable p^* is the most computationally intensive term because of the exponentials in p and ρ in (2.19). However, for fully isentropic flow, and also outside shock regions, p^* is constant. Since p^* appears in the expression for w_i and the reciprocal of p^* in $\tilde{f}_i$ it follows from (2.23) that in those cases p^* is canceled and the computations simplify. We use this simplification on all grids that do not contain shocks. Also, as shown above, the computation of the exponential terms is faster for several values of α, e.g., $\alpha = 1$ and $\alpha = 1 - 2\gamma$. We remark that because of the simplicity of (2.17) and the expression for the Jacobian $\tilde{f}_w$, all computations are done in the conservative variables and shuffling back and forth between symmetrized and conservative variables is not needed.

2.4. *Nonconservative Form*

It is well known that if a scheme is in conservative form, the computed shock speeds will be correct (see, e.g., [12]).

This condition is sufficient, but not necessary. Tadmor [28] showed how to obtain second-order schemes for initial-boundary value problems that are entropy stable and in conservative form. It is, however, unknown if such schemes exist for higher orders of accuracy. The SHOEC scheme (2.23) is not written in conservative form. To check the shock speed, we computed the numerical solution for a single moving shock of varying strength. We used long time integration with the number of time steps of the order $O(10^3)$ and a sequence of decreasing grid sizes h, where h varied from $h = 2 \times 10^{-1}$ to $h = 2 \times 10^{-4}$. In all cases, the computed location of the shock was found to be within the correct grid-cell and thus to converge with h.

3. ARTIFICIAL VISCOSITY

Around shocks we introduce a sequence of refined grids on which we supplement the scheme with an artificial viscosity term to control spurious oscillations. Ideally, this should be done such that

1. the stability estimates are not destroyed
2. there is no loss of accuracy near the shock
3. shocks are resolved sharply
4. the artificial viscosity terms can be computed cheaply.

We discuss each of these items below.

A natural choice for the artificial viscosity term is a properly scaled discretization of a diffusion term $(Eu_x)_x$, which arises in many applications. Here, $E = E(u)$ is a positive definite matrix. For high order schemes, discretizations of higher order viscosity terms like $(-1)^{r-1}$ $(\partial^r/\partial x^r)(E(\partial^r u/\partial x^r))$ are sometimes used, or combinations of lower and higher order terms. Examples of such blended artificial viscosity terms are given in [5, 7]. In the former, Gustafsson and Olsson used the augmented conservative central scheme scheme

$$\boldsymbol{u}_t = -D\boldsymbol{f} + hQ\boldsymbol{u}, \tag{3.1}$$

where the artificial viscosity term is given by

$$hQ\boldsymbol{u} = hR_{2r}D_+ E D_- \boldsymbol{u}. \tag{3.2}$$

The operators D and R_{2r} are given by (2.24) and (2.25), and the matrix E contains the blocks $E(u_j)$. In their paper a scalar artificial viscosity $E = \varepsilon I$, $\varepsilon > 0$ is derived that leads to one-point shocks for scalar equations. The choice of artificial viscosity (3.2) ensures that the sharp shock resolution is obtained for all orders of accuracy $2r$. For the second-order SHOEC scheme we use the discrete artificial viscosity

$$hQ\boldsymbol{w} = hD_+ Eu_w D_- \boldsymbol{w}. \tag{3.3}$$

Again, this is a consistent discretization of $(Eu_x)_x$ which can be written as $(Eu_w w_x)_x$. In contrast to (3.2), it can be shown that (3.3) preserves the stability estimates. We can demonstrate this by taking the innerproduct of (3.3) with $\boldsymbol{w}$. Assuming that $E_j = 0$ at the boundaries of the domain,[1] we get

$$h(\boldsymbol{w}, D_+ Eu_w D_- \boldsymbol{w}) = -h(D_-\boldsymbol{w}, Eu_w D_-\boldsymbol{w}). \tag{3.4}$$

This term is nonpositive and therefore has the correct sign, if Eu_w is positive definite. We remark that positive definiteness is obtained for all scalar viscosities $E = \varepsilon I$, as u_w is positive definite. The addition of the artificial viscosity term (3.3) reduces the SHOEC scheme to first order. For $r > 1$ we could generalize (3.3) to

$$hQ\boldsymbol{w} = \begin{cases} h(h^2 D_+ D_-)^{(r-1)/2} D_+ Eu_w D_- (h^2 D_+ D_-)^{(r-1)/2}\boldsymbol{w}, & r \text{ odd}, \\ -h^{-1}(h^2 D_+ D_-)^{r/2} Eu_w (h^2 D_+ D_-)^{r/2}\boldsymbol{w}, & r \text{ even}, \end{cases} \tag{3.5}$$

which would result in a scheme of order $(2r-1)$. However, Sjögreen [26] recently found that any scheme for systems of conservation laws will reduce to first-order accuracy at shocks. The simpler viscosity (3.3) therefore suffices. Sjögreen's find also means that the high order of accuracy of a scheme can only be retained if the grid is refined in the shock region. This is exactly what we are doing. We note that we implement the viscosity only locally around the discontinuity. Its location is returned by the wavelet detection algorithm discussed in the next section.

Having satisfied the first two criteria for the artificial viscosity terms, it remains to discuss how to construct a cheap artificial viscosity that leads to sharp shock resolutions. For computational efficiency, we are primarily interested in scalar viscosities for which $E = \varepsilon I$. Below, we derive a value for ε that gives approximate one point shocks for weak shocks and sharp resolution for strong shocks. The extra point is needed in practice to allow for the representation of shocks that are not positioned in the center of a grid cell. We remark that any (larger) positive scalar viscosity can be used if it is implemented as shown above, as long as the refined grids on which the artificial viscosity is applied is sufficiently fine.

Following the approach in [5] we consider finite difference solutions of (2.1) with the Riemann initial condition

$$u(x,0) = \begin{cases} u_l, & x < 0 \\ u_r, & x \geq 0. \end{cases} \tag{3.6}$$

[1] Note that D_+ and D_- do not satisfy the summation-by-parts principle (B.1).

The shock states u_l and u_r are connected by a k-shock and satisfy the Lax entropy conditions

$$\lambda_k(u_l) > s > \lambda_k(u_r), \quad \lambda_{k-1}(u_l) < s < \lambda_{k+1}(u_r), \quad k = 1, 3.$$

Here, $\lambda_1 = (v - c)$, $\lambda_2 = v$, and $\lambda_3 = (v + c)$ are the characteristic speeds.

For simplicity, we furthermore assume that u_l is the downstream (supersonic) shock state and that the flow is in the positive x-direction so that $\lambda_k = v - c$. For such problems, the scalar artificial viscosity is often chosen proportional to $\max_i|\lambda_i(\overline{u}) - s|$, where $\overline{u}$ is some average of u_l and u_r. Johansson and Kreiss [10] show that this viscosity indeed suppresses spurious oscillations, but leads to excessive smearing. Instead, we will show below that $\varepsilon = \min_i|\lambda_i(\overline{u})|$ gives good results for stationary shocks and that $|\lambda_2(\overline{u}) - s|$ or $\max_i|\lambda_i(\overline{u}) - s|$ are suitable for moving shocks or very strong stationary shocks.

We apply the coordinate transformation ($y = x - st$, $\tau = t$) to (2.1) which then changes to the stationary problem

$$(f - su)_y = 0,$$
$$u(y, 0) = \begin{cases} u_l, & y < 0, \\ u_r, & y \geq 0, \end{cases} \tag{3.7}$$

since $u_\tau = 0$ in the (y, τ)-coordinates. Adding constant scalar artificial viscosity we discretize (3.7) as

$$D_0(f_j - su_j) = h\varepsilon D_+ D_- u_j. \tag{3.8}$$

or

$$f_{j+1} - f_{j-1} - s(u_{j+1} - u_{j-1}) = 2\varepsilon(u_{j+1} - 2u_j + u_{j-1}). \tag{3.9}$$

We want to design ε to support viscous shock profiles consisting of the states u_l, u_r, and one intermediate state u_m.[2] We obtain the following equations at the points $x = -h$, $x = 0$, and $x = h$:

$$f_m - f_l - s(u_m - u_l) = 2\varepsilon(u_m - u_l), \tag{3.10}$$
$$f_r - f_l - s(u_r - u_l) = 2\varepsilon(u_r - 2u_m + u_l), \tag{3.11}$$
$$f_r - f_m - s(u_r - u_m) = 2\varepsilon(u_m - u_r). \tag{3.12}$$

At all other grid points, the equations are trivially satisfied. The left-hand side of (3.11) vanishes because of the RH conditions which gives $u_m = (u_r + u_l)/2$. As $f_r = f_l + s(u_l - u_r)$, Eqs. (3.10) and (3.12) are in fact identical. For the Euler equations, however, Eq. (3.10) cannot be satisfied *exactly* for scalar viscosities ε (see also [9]). Consider the equation corresponding to the first element of the flux vector in (3.10):

$$\rho_l v_l - \rho_m v_m = (2\varepsilon + s)(\rho_l - \rho_m). \tag{3.13}$$

We have $\rho_m = (\rho_l + \rho_r)/2$ and $\rho_m v_m = (\rho_l v_l + \rho_r v_r)/2$. Consequently,

$$\rho_l v_l - \rho_r v_r = (2\varepsilon + s)(\rho_l - \rho_r). \tag{3.14}$$

The RH conditions require $\rho_l v_l - \rho_r v_r = s(\rho_l - \rho_r)$, and so $2\varepsilon(\rho_l - \rho_r) = 0$, which cannot be fulfilled for $\varepsilon > 0$. Equations (3.10) and (3.12) lead to

$$f_m - f_l = (s + 2\varepsilon)(u_m - u_l), \tag{3.15}$$
$$f_r - f_m = (s - 2\varepsilon)(u_r - u_m). \tag{3.16}$$

We see that Eq. (3.15) represents a k-shock between states u_l and u_m moving with speed $(s + 2\varepsilon)$, while (3.16) represents a k-shock between states u_m and u_r moving with speed $(s - 2\varepsilon)$. The interaction between two such shocks generally results in the formation of a k-shock between u_l and u_r as well as a contact discontinuity and a rarefaction wave [1], whence the above described conflict for the Euler equations. But for weak shocks, (3.15) and (3.16) will be approximately satisfied. Using Roe-linearization Eq. (3.15) becomes

$$A(u_{ml})(u_m - u_l) = (s + 2\varepsilon)(u_m - u_l),$$

where $A(u_{ml})$ is the Jacobian matrix f_u evaluated at the Roe-averaged state-vector u_{ml} determined by u_l and u_m [23]. Thus, $(u_m - u_l)$ is an eigenvector of $A(u_{ml})$ with eigenvalue $(s + 2\varepsilon) = \lambda_k(u_{ml})$, or

$$\varepsilon = 1/2(\lambda_k(u_{ml}) - s)$$

to the left of the shock. Similarly, $\varepsilon = 1/2(s - \lambda_k(u_{rm})) \approx 1/2(\lambda_k(u_{ml}) - s)$ to the right of the shock. This choice of scalar artificial viscosity corresponds to that used by Jameson in [9]. Since $\lambda_k(u_l) > s$, $\lambda_k(u_{lr}) = s$ and the jump $[u_l - u_m]$ is less than the jump $[u_l - u_r]$, it can be expected that $\lambda_k(u_{lm}) > s$ also. In practical applications we set $\varepsilon = 1/2|\lambda(u_{lm})_k - s|$. We note that $|\lambda_k(u_{ml}) - s| = \min_i|\lambda_i(u_{ml}) - s|$. Similar analyses for other flow situations lead to the same choice

$$\varepsilon = 1/2 \min_i |\lambda_i(u_{mp}) - s|, \tag{3.17}$$

[2] Note that (3.9) does not support zero-point shocks for $\varepsilon > 0$. The left-hand side of (3.9) vanishes because of the RH conditions. This leads to $\varepsilon(u_l - u_r) = 0$, which can only be satisfied for $u_l = u_r$.

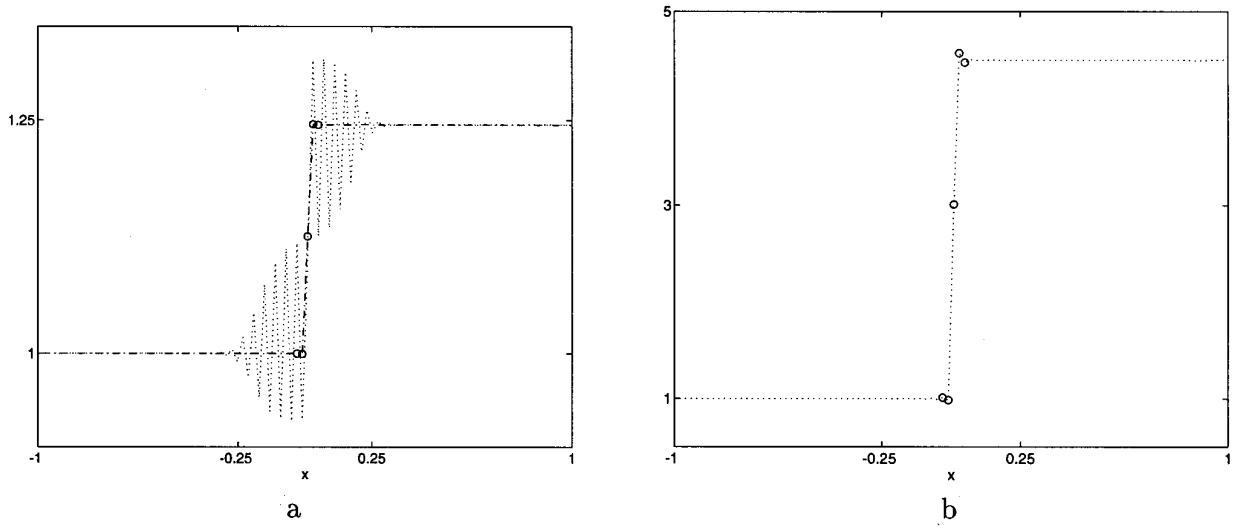

FIG. 1. Pressure for stationary shock problem at $t = 2$, both second-order conservative and second-order SHOEC scheme with $E = \varepsilon I$ and ε given by (3.17): (a) $M = 1.1$: with viscosity (–.); no viscosity (·); (b) $M = 2$: with viscosity (·).

where u_p is the upstream state. For scalar equations, Eqs. (3.10), (3.11), and (3.12) are satisfied exactly for the above artificial viscosity. We note that also for systems (3.10) can be satisfied exactly if the matrix viscosity $E = (A(u_{lm}) - sI)/2$ is used. However, this matrix E is not symmetric. So, even if its eigenvalues are all positive, it is not necessarily positive definite.

We show the effectiveness of the artificial viscosity (3.17) for *stationary* shocks in Figs. 1a and 1b. They depict the pressure after long time integration. Both the second-order conservative scheme, given by (3.1) and (3.2), as well as the second-order SHOEC scheme with (3.3) were tested. The results were identical. The computations are done for $n = 100$, a CFL number of 0.5 and Mach numbers $M = 1.1$ and $M = 2$ without local grid adaptation. The numerical solutions are indicated by dotted lines, and points in the shock region are circled. The solutions have negligible small amplitude oscillations even for high Mach numbers, although the derivation of the scalar viscosity was based on a weak shock assumption. Similar results are obtained for higher order ($r = 2, 3$) SHOEC methods with (3.5).

Moving Shocks

Above, the equations are discretized on a grid that moves along with the shock, which is not the case in reality. Results for scalar equations are still satisfactory [5]. But, the damping by the viscosities is insufficient for the Euler equations if the shock speed s is not identically zero, and a larger viscosity is needed. In the experiments whose results are shown in Section 5 we used

$$\varepsilon = \tfrac{1}{2}|\lambda_2(u_{ml}) - s|, \tag{3.18}$$

where $\lambda_2 = v$, instead of (3.17) for moving shocks. The shock speed s is computed using the approximation $s \approx (\lambda_k(u_l) + \lambda_k(u_r))/2$. If oscillations are still present, which can be detected easily by the algorithm discussed in the next chapter, we resort to the common and larger scalar viscosity $\max_i|\lambda_i(u_{ml}) - s|$ mentioned earlier. We remark that in the experiments the artificial viscosity is only used on the locally refined grids so that excessive smearing does not occur at the coarse grid scale. In fact, we can use as large an artificial viscosity as we want, as long as we keep the refined grids on which it is added sufficiently fine.

4. DETECTION WITH WAVELETS

We want to detect shocks and spurious oscillations to aid the local grid adaptation procedure. The detection algorithm is based on a wavelet analysis of the pressure grid function. In the first part of this section we give a brief introduction to discrete wavelet families (4.1), motivate the choice of wavelet family and explain how the local behavior of a function can be determined from its wavelet transforms (4.2). The second part deals with implementation issues. The fast wavelet transform (FWT) algorithm, introduced in 4.3, makes the detection algorithm computationally attractive. In 4.4 we discuss the implications of discrete grid functions, finite domains and the presence of spurious oscillations. At the end of the section we give a general outline of the detection algorithm. Here, we focus on issues that are relevant in the context of numerical analysis. For a detailed description of the algorithm, including pseudo-code, we refer to [3]. We recommend Daube-

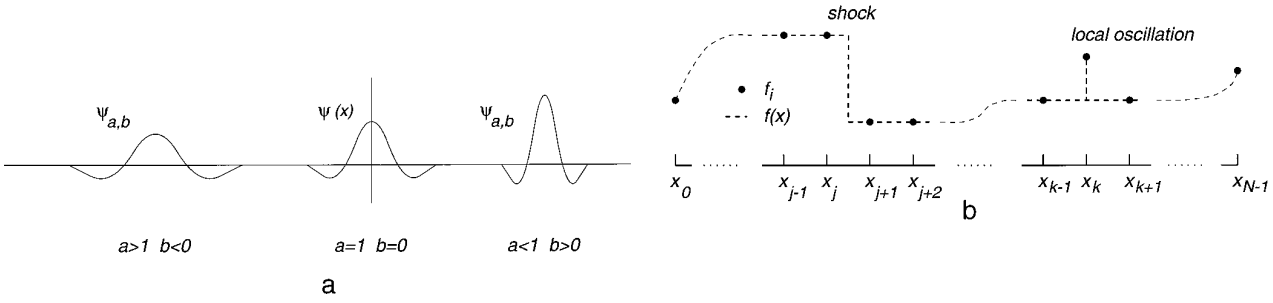

FIG. 2. (a) Different members of the wavelet family; (b) example of discrete function f_i and the corresponding continuous function $f(x)$.

chies' book [2] for a thorough mathematical discussion of wavelet theory. The wavelet families used in the detection algorithm and the underlying mathematical theory were developed by Mallat, Hwang, and Zhong in [15–17].

4.1. *Wavelets and Discrete Wavelet Families*

Roughly speaking a wavelet $\psi(x)$ is a well localized function that "waves" above and below the x-axis such that $\int \psi(x)\, dx = 0$.[3] Dilations by $a \in \mathbb{R}^+$ and translations by $b \in \mathbb{R}$ of the mother wavelet $\psi(x)$ generate the wavelet family

$$\psi_{a,b}(x) \equiv \frac{1}{a}\,\psi\left(\frac{x-b}{a}\right). \tag{4.2}$$

The parameter b is the *center* of the wavelet $\psi_{a,b}$, and a represents its *scale*. A mother wavelet $\psi(x)$ and two members of the corresponding wavelet family are depicted in Fig. 2a. For $a > 1$ the wavelet $\psi_{a,b}$ stretches and can be viewed as representing a lower frequency, while for $a < 1$ the wavelet narrows and represents a higher frequency. Thus, the concepts of scale and frequency are closely related.

The continuous wavelet transform of a function $f \in L^2$ is given by

$$\langle f, \psi_{a,b}\rangle = \frac{1}{a}\int f(x)\,\psi\left(\frac{x-b}{a}\right) dx, \quad a \in \mathbb{R}^+, b \in \mathbb{R} \tag{4.3}$$

The variables $\langle f, \psi_{a,b}\rangle$ are referred to as the wavelet coefficients and give information on the frequency content of f near the points b.

For all practical purposes we are, of course, only interested in discrete values for a and b. The dilation parameter a is discretized as $a_m = 2^m$, $m \in \mathcal{Z}$, where m represents the level. The corresponding families $\psi_{2^m,b} = 2^{-m}\psi((x - b)/2^m)$ are referred to as *dyadic* wavelet families and facilitate the formulation of fast wavelet transform (FWT) algorithms (Section 4.3)

At each level m the wavelet coefficients are computed at the centers $b_{m,n} = n\Delta b$, $n \in \mathcal{Z}$, where Δb may depend on m. This gives

$$\psi_{m,n} \equiv \psi_{2^m, b_{m,n}} = 2^{-m}\,\psi\left(\frac{x - n\Delta b}{2^m}\right), \quad m \in \mathcal{Z}. \tag{4.4}$$

To ensure that the wavelet coefficients contain enough information to characterize f, the family consisting of the wavelets $\psi_{m,n}$ must constitute a *frame* [2]; i.e., there exist $0 < A \le B < \infty$ such that for all $f \in L^2$,

$$A\|f\|^2 \le \sum_{m,n\in\mathcal{Z}} |\langle f, \psi_{m,n}\rangle|^2 \le B\|f\|^2.$$

The case when $A = B = 1$ corresponds to $\{\psi_{m,n}\}$ being a basis. The choice of the mother wavelet $\psi(x)$ and the discretization of b are essentially only restricted by the frame and the admissibility conditions. The mother wavelet is normally chosen such that it is well concentrated in both the spatial and the frequency domain.

The detection algorithm is based on a wavelet analysis of the pressure grid function given by the discrete function f_i, $i = 0, \ldots, N - 1$. Consequently, m and n are bounded; the smallest scale that can be considered is determined by the grid size h, the largest scale is determined by the size of the domain, and the maximum number of points at which the wavelet coefficients can be evaluated is equal to N. Throughout this section, f_i is assumed to be the discrete representation of the function $f(x)$, $x \in [x_0, x_{N-1}]$. To facilitate the discussion of the wavelet theory we consider functions $f(x)$ that can contain discontinuities at $x =$

[3] Formally, a function $\psi(x)$ is said to be a wavelet if and only if its Fourier transform $\hat{\psi}(\omega)$ satisfies

$$\int_0^{+\infty} \frac{|\hat{\psi}(\omega)|^2}{\omega}\, d\omega = \int_{-\infty}^{0} \frac{|\hat{\psi}(\omega)|^2}{|\omega|}\, d\omega = C_\psi < +\infty. \tag{4.1}$$

This *admissibility condition* requires the wavelet to have sufficient decay in the frequency domain and that $\hat{\psi}(0) = 0$, which in turn leads to $\int \psi(x)\, dx = 0$.

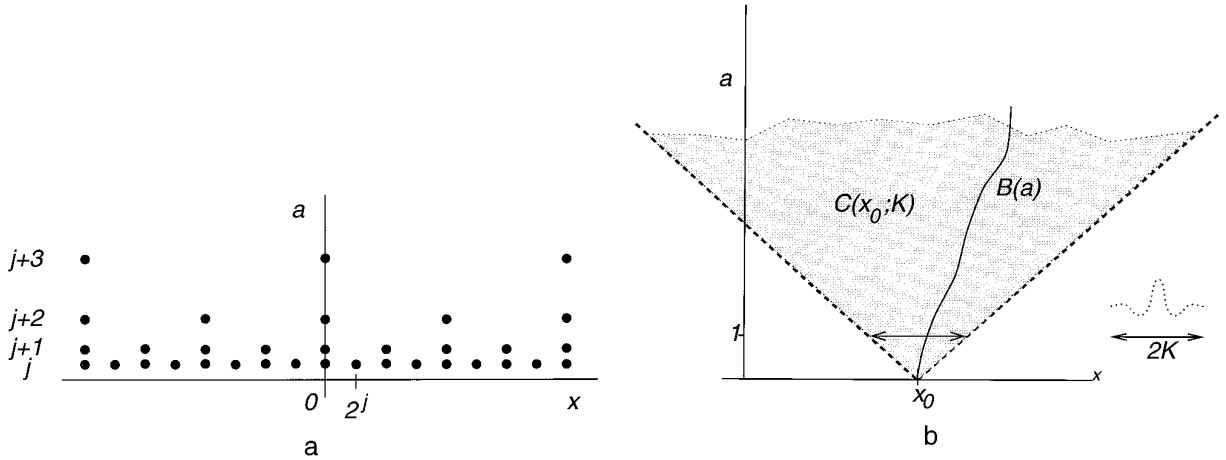

FIG. 3. (a) Lattice of wavelet centers for orthogonal families; (b) cone of influence of x_0.

$x_{j+1/2}$, represented in the discrete domain by a jump between f_j and f_{j+1}, and local oscillations at $x = x_k$ when $(f_{k+1} - f_k) * (f_k - f_{k-1}) < 0$. Otherwise $f(x)$ is assumed to be slowly varying. An example is given in Fig. 2b. In Section 4.4 we discuss grid functions that do not adhere to these simplifications, such as smeared shocks, grid functions with spurious oscillations around shocks, and grid functions that vary sharply in the vicinity of a shock.

4.2. *Selection of the Discrete Wavelet Family*

The wavelet family is selected based on two criteria:

1. There must exist a clear relation between the behavior of the wavelet coefficients and the local regularity of $f(x)$.

2. The ensuing algorithm must be efficient; i.e., the number of wavelet coefficients needed to determine the local regularity of $f(x)$ with sufficient accuracy should be small.

For very special choices of $\psi(x)$ and with $\Delta b = 2^m$, the wavelet family $\psi_{m,n}$ constitutes an orthonormal basis. Many popular wavelet families, e.g., the Haar, Daubechies, or Meyer wavelets, are members of this class. The orthogonal families satisfy the first criterion [2] but fail to meet the second in this application. To understand this, we observe that shocks and local oscillations may travel through the flow domain. The detection results should not depend on the position of the shocks or oscillations, in other words, the wavelet transform should be *shift-invariant.* Figure 3a shows the centers in part of the (a, x) space at which wavelet coefficients $\langle f, \psi_{m,n} \rangle$ are computed in an orthogonal wavelet analysis. This lattice is the same for all dyadic orthogonal wavelet families. We assume that f has a bounded discontinuity at $x_s = 0$, at which wavelet coefficients are computed at each scale. If the function is shifted by a distance of, for example, 2^j, only one wavelet coefficient is computed at the new location $x_s = 2^j$ at the levels shown. Also, the wavelet coefficients evaluated at positions close to x_s change as x_s is shifted. In practice, only a finite number of levels can be evaluated, and we expect that the detection results, which are based on this limited information, will change as well. Daubechies shows that indeed a very large number of levels is needed to accurately determine the true local behavior of the function for shifted singularities. Specifically, coefficients are needed at scales close to, or smaller than, the shift, which may not be available. So, orthogonal families are not suitable for detection purposes in the context of this paper; shift-dependency is unacceptable.

Clearly, shift dependency can be avoided if the wavelet coefficients are computed at the same points at all scales, in other words, if $\Delta b = \text{const}$. This constant, which represents the smallest scale possible, is determined by the grid size. Because the grid size h is not necessarily equal to a power or inverse power of 2, we normalize the smallest scale h to 1 (corresponding to $m = 0$). Then, $\Delta b \equiv 1$ in (4.4), which gives

$$\psi_{m,n} = 2^{-m} \psi\left(\frac{x - n}{2^m}\right), \quad m \geq 0. \tag{4.5}$$

This normalization is used in the remainder of the paper.

Having thus abandoned orthogonality, freedom in the design of the mother wavelet is gained. The question is if this freedom can be used to construct nonorthogonal families that satisfy the two criteria given above. Mallat and Hwang [16] showed that this is possible if the mother wavelet $\psi(x)$ has compact and symmetric support $[-K, K]$ for $K > 0$, and if it is a derivative of a smoothing function. From now on, all mother wavelets are assumed to be in this class. A smoothing function $\theta(x)$ is defined as a differentiable function that satisfies

$$\theta(x) > 0, \quad \int \theta(x)\, dx = 1; \quad \lim_{x \to \pm\infty} \frac{d^k \theta(x)}{dx^k} = 0, \quad k = 1, 2, \ldots . \tag{4.6}$$

From (4.6) it follows that $\int \psi(x)\, dx = 0$ for $\psi(x) \equiv d^k\theta/dx^k$ with $k > 0$. Provided $\psi(x)$ has sufficient decay in the frequency domain, it will satisfy the admissibility condition (4.1).

For such mother wavelets the local regularity of $f(x)$ can be computed from a small and easy-to-determine set of wavelet coefficients. The local regularity of a function is measured in terms of its Lipschitz exponent α, whose definition is given in appendix C. From this definition it follows that a continuous function has a Lipschitz exponent $\alpha > 0$, a bounded discontinuity (shock) is Lipschitz 0, and a Dirac function (local oscillation) has a Lipschitz exponent $\alpha = -1$. For ease of presentation, the theorem is presented for continuous wavelet families $\psi_{a,b} = (1/\alpha)\psi((x - b)/a)$, $a \in \mathbb{R}^+$, $b \in \mathbb{R}$. First we make the following observation. If the support of the mother wavelet ψ is equal to $[-K, K]$, $\psi_{a,b}$ has support $[b - Ka, b + Ka]$. Thus, at any scale a, the function value $f(x_0)$ will influence the wavelet coefficients $\langle f, \psi_{a,b}\rangle$ computed at the centers b in the set

$$S(a, x_0; K) \equiv \{b : |b - x_0| \le Ka\}. \tag{4.7}$$

The region $C(x_0; K) \equiv \bigcup_a \{a\} \times S(a, x_0; K)$ is referred to as the *cone of influence* of x_0 (Fig. 3b). It is intuitive to think that the local regularity of f at x_0 should be determined by the wavelet coefficients evaluated at centers in $C(x_0; K)$. Mallat and Hwang [16] proved that this is true for the functions $f(x)$ considered in this paper. Mallat strengthened the result further in the following theorem:

THEOREM 4.1. 1. *Let θ be a smoothing function and let $\psi^k(x) = d^k\theta(x)/dx^k$, $k > 0$ have compact support $[-K, K]$. Let $b = B(a)$ be a curve in the cone of influence of x_0, with $B(a) \to x_0$ as $a \to 0$ (figure 3b). The function f is Lipschitz $\alpha < k$ at x_0, if there exists a constant $C > 0$ and a scale $\tilde{a}$ such that along any $B(a)$,*

$$|\langle f, \psi_{a,b}\rangle| \le Ca^\alpha, \quad \forall a < \tilde{a}. \tag{4.8}$$

2. *Define a modulus maximum at the scale a as a local maximum of $|\langle f, \psi_{a,b}\rangle|$ in b. The points b at which the modulus maxima are attained are referred to as the maximum points at scale a. If f has an isolated discontinuity at x_0, there exist a scale $\tilde{a}$ and a curve $b = B_M(a)$ such that for all $a < \tilde{a}$, $B_M(a)$ are maximum points. Such curves are referred to as maximum lines. The Lipschitz exponent of f at x_0 is determined by* (4.8) *evaluated along the maximum lines converging to x_0.*

A similar theorem also holds for dyadic families, with $a_m = 2^m$, and $b \in \mathbb{R}$ [18, 17]. However, we cannot compute coefficients at scales smaller than 1, nor at positions other than the grid points. Thus, we presume that the decay of the available wavelet coefficients at scales larger than 1 characterizes the regularity of the function. If this is not the case, the mesh must be refined (decreasing h). The second part of the theorem makes the wavelet detection computationally attractive; the Lipschitz exponent α at a point x_0 can be estimated from a limited number of wavelet coefficients. At a sequence of levels m, where $1 \le m \le m_{\max} \le \log_2(N)$, we compute the wavelet coefficients at the grid points. Next, we find the modulus maxima at each level and locate maximum lines that converge on the scale of the grid. Then, we determine α such that

$$\log_2 |\langle f, \psi^k_{m,n}\rangle| = \log_2 C + m\alpha, \tag{4.9}$$

as close as possible, in a least squares sense, for the wavelet coefficients along the select maximum lines.

As an example, Fig. 4a shows a signal with several points of distinct behavior, and the modulus maxima computed with the detection algorithm at increasing levels j, $j + 1, \ldots$. If the Lipschitz exponent α is positive, the amplitude of the modulus maxima increases with j. The smooth variation points 1 and 4 exhibit this behavior. The singularity at 3 produces modulus maxima that decrease as the scale increases, so $\sup(\alpha) < 0$. The amplitudes of the modulus maxima corresponding to point 2 do not change and we conclude that $\sup(\alpha) = 0$.

The parameter k limits the maximum Lipschitz exponent that can be determined. As we are interested in detecting discontinuities ($\alpha = 0$) and spurious oscillations ($\alpha < 0$), we choose $k = 1$. We remark that for $k = 1$, a direct connection exists between the wavelet detection and detection algorithms that search for maxima in derivatives. Define $\theta_{a,b} \equiv a^{-1}\theta((x - b)/a)$. The function $\theta_{a,b}$ is a smoothing function as $\int \theta_{a,b}(x)\, dx = \int \theta(x)\, dx = 1$. Also,

$$\psi_{a,b} = a \frac{d\theta_{a,b}}{dx},$$

so that

$$\langle f, \psi_{a,b}\rangle = \left\langle f, a \frac{d\theta_{a,b}}{dx} \right\rangle = -a \frac{d}{db} \langle f, \theta_{a,b}\rangle. \tag{4.10}$$

In other words, the wavelet transform is the first derivative of the function f smoothed at the scale a by $\theta_{a,b}$. So, detecting modulus maxima corresponds to detecting maxima in derivatives. It follows that a discontinuity has one maximum line converging to its location as the derivative of the smoothed function will have an absolute maximum at

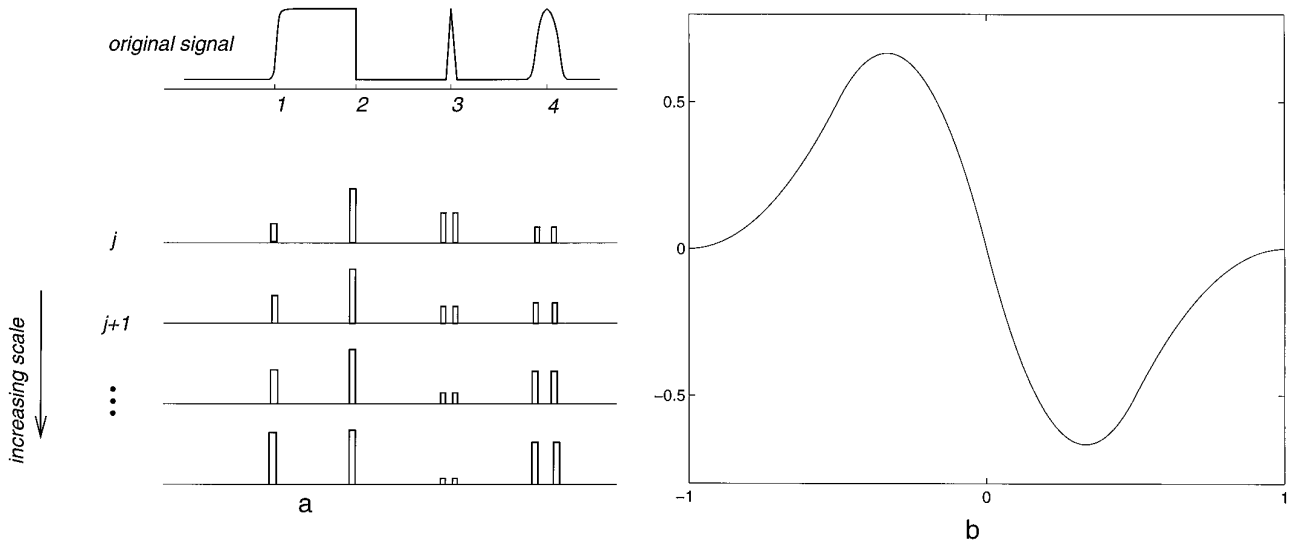

FIG. 4. (a) Example wavelet transformation; (b) the spline wavelet ψ.

this position. A Dirac function naturally has two maximum lines. Furthermore, we note that the wavelet coefficients provide an estimate of the *jump* $[f]_a$ at scale a across the shock:

$$|[f]_a| = a\,\frac{|[f]_a|}{a} \approx a\left|\frac{d\langle f, \theta_{a,b}\rangle}{db}\right| = |\langle f, \psi_{a,b}\rangle|, \quad (4.11)$$

which can be used as an extra criterion for shock selection.

4.3. *The Fast Wavelet Transform*

For special $\psi(x)$ the wavelet transformations can be performed through fast discrete filter operations [3, 17]. Given two sequences $\{g_k\}_k$ and $\{h_k\}_k$, we define $G_m \equiv \{g_l^m\}_l$ and $H_m \equiv \{h_l^m\}_l$ as the sequences constructed by putting $(2^{m-1} - 1)$ zeros between the elements of, respectively, $\{g_k\}_k$ and $\{h_k\}_k$. Also, $W_m \equiv \{\langle f, \psi_{m,n}\rangle\}_n$ is defined as the sequence of wavelet coefficients at level m. It can be shown that certain $\psi(x)$ possess sequences $\{g_k\}_k$ and $\{h_k\}_k$ such that the wavelet coefficients at the levels $m \geq 1$ can be computed by the discrete convolutions

$$\begin{aligned} W_m &= \frac{1}{\lambda_m} G_m * S_{m-1}, \\ S_m &= H_m * S_{m-1}, \quad m = 1, 2, \ldots, \end{aligned} \quad (4.12)$$

where the sequence S_0 contains the grid function values f_i. The sequences S_m represent smoothed versions of f at level m, whereas W_m can be seen as representing the details lost in this smoothing process. For this reason, the sequence $\{h(k)\}_k$ is referred to as the impulse response of a *low pass* filter and $\{g(k)\}_k$ as the impulse of a *high pass* filter. The finite resolution of $f(x)$ necessitates the scaling by the parameters λ_m. If the sequences S_m were available at all levels $m < 0$ (for $a_m \to 0$), the scaling parameters would not be needed. We refer to [3] for full details concerning their derivation. At each level m, we perform $O(n)$ operations. The maximum number of levels is equal to $\log_2(n)$. For detection purposes it is sufficient to compute the wavelet coefficients at a total of four or five levels. Therefore, the overall detection algorithm is $O(n)$. In the detection algorithm we use the mother wavelet depicted in Fig. 4b. It is a quadratic, antisymmetric spline with compact support $[-1, 1]$ given by

$$\psi(x) = \begin{cases} 2(x+1)^2, & -1 \leq x < -\frac{1}{2}, \\ -4x(1+x) - 2x^2, & -\frac{1}{2} \leq x < 0, \\ -4x(1-x) + 2x^2, & 0 \leq x < \frac{1}{2}, \\ -2(x-1)^2, & \frac{1}{2} \leq x < 1. \end{cases} \quad (4.13)$$

Its filter coefficients h_k and g_k, and the scaling parameters λ_m are given in Table I. Note that symmetry is obtained by applying a shift of 1/2 to W_m.

4.4. *Implementation Issues*

The pressure grid function f_i may be distorted by spurious oscillations around the shock. They are characterized by wavelength L, $L \geq 2h$ and amplitude r. Figure 5a shows the damping factors r_H/r and r_{HH}/r, where r_H and r_{HH} are the amplitudes of the smoothed oscillations after respectively one and two applications of H. Oscillations with a

TABLE I

Filter Coefficients and Scaling Parameters for the Spline Wavelet

Filter coefficients			Scaling parameters			
k	h_k	g_k	m	λ_m	m	λ_m
−1	0.125		1	2	5	1.336
0	0.375	−2.0	2	1.5	6	1.334
1	0.375	2.0	3	1.375	7	1.333
2	0.125		4	1.344	>7	1.333

wavelength $L = 2h$ are removed immediately, and oscillations with short wavelengths are dampened quickly. Therefore, the oscillations have little and negligible effect on the computation of the Lipschitz coefficient α if we use levels $m \geq 2$ in (4.9). An example is given in Fig. 5b. It shows a pressure distribution obtained from a central finite difference scheme applied to the Euler equations. The oscillations are prominent at the smallest scale but quickly disappear. Note that the jump $|[f]|$ across the shock is accurately represented by the wavelet coefficients.

If a shock is smeared, the estimated Lipschitz exponent will be larger than zero. However, as the scale increases, the modulus maxima will quickly converge to a constant, equal to the total jump over the smeared shock. For one- and two-point shocks, the correct Lipschitz exponent can generally be detected from the modulus maxima at the levels $m \geq 3$. Otherwise, local oscillations and/or large magnitudes of the wavelet coefficients at the larger scales will indicate that there is a steep gradient necessitating local grid refinement. We remark that as a result of local grid refinement and an efficient artificial viscosity, smearing is generally not an issue at the coarser scales.

If the grid function varies sharply close to a discontinuity, the Lipschitz exponent will also be perturbed. However, the grid adaptation procedure will refine the grid locally as the detection algorithm will pick up local oscillations. At the finest scales, the variation in the grid function close to the shock will not be as strong and the discontinuity can again be detected with sufficient accuracy.

As the discrete domain is finite, we need to periodize f_i. To avoid the introduction of artificial shocks at the boundary, the finite discrete domain is extended by reflection according to

$$f_i = f_{2n-i} \quad \text{for } n < i \leq 2n - 1. \tag{4.14}$$

Although the reflected image is continuous at the boundary, its derivative may not be so. At the boundary itself this will not cause any problems because the filter G is antisymmetric. In the local grid adaptation procedure, we ensure that the shocks are located in the interior of the (refined) grids and that the flow varies smoothly near the boundaries. Therefore, the cusp or kink resulting from a discontinuous boundary derivative will be very small and will have negligible effect on the wavelet coefficients in the domain interior.

Approximations to the shock states u_l and u_r are needed to construct the artificial viscosity. If no local spurious oscillations are present, this task is trivial once the shock location is known. Otherwise, the data at the scale of the

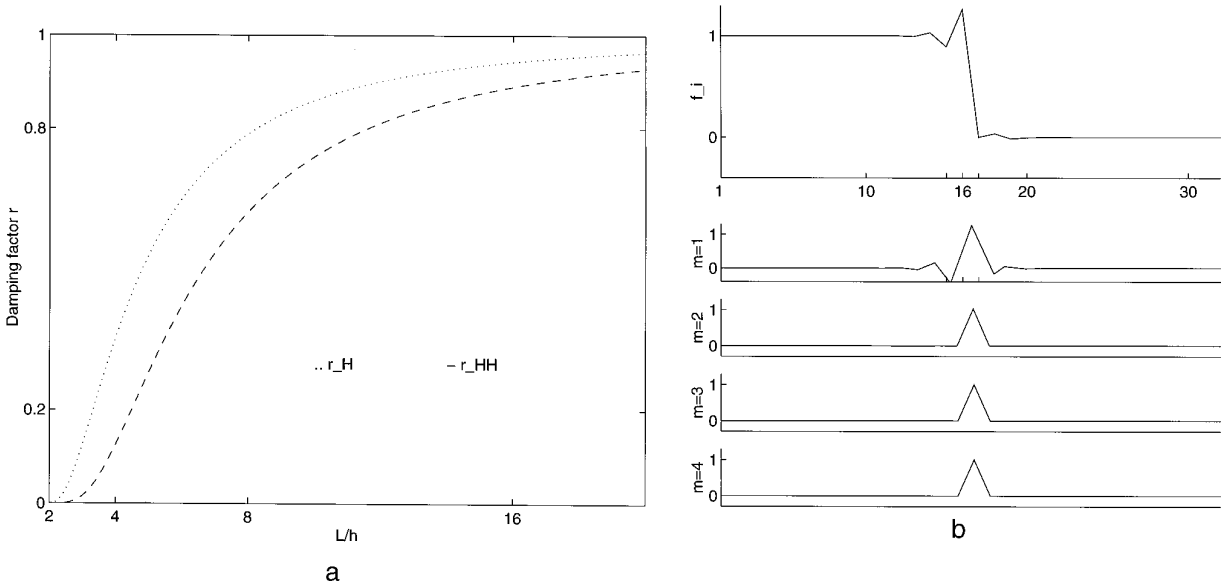

FIG. 5. (a) Damping factors filter H; (b) maxima wavelet coefficients $\langle f, \psi_{m,n} \rangle$ corresponding to an oscillatory grid function f_i.

TABLE II

General Outline of the Detection Algorithm

	Reference
Periodize the grid function f_i by reflection	Eq. (4.14)
Compute $\langle f, \psi_{m,n} \rangle$ in the extended domain at the scales $a_m = 2^m$, $m = 1, ..., m_{\max}$ with a fast wavelet transform	Eqs. (4.12), Table 1
Locate the maxima $\lvert\langle f, \psi_{m,n}\rangle\rvert$ at each scale	
Determine the converging maximum lines	Theorem (4.1)
Compute the Lipschitz exponents from the evolution of the wavelet coefficients along the converging maximum lines	Eq. (4.9)
Locate shocks, sharp gradients, and spurious oscillations	Sec. 4.2, 4.4

grid is distorted and we approximate f_L and f_R from the smoothed data S_m at scales $m \geq 1$.

We summarize the findings concerning the choice of the wavelet family:

- The family is dyadic for computational purposes.
- The family is redundant to obtain shift-invariance.
- The mother wavelet is compact, differentiable, and the first derivative of a smoothing function so that Theorem 4.1 is valid.
- A fast wavelet transform exists, leading to an $O(n)$ detection algorithm.

In Table II a general outline of the detection algorithm is given with references to the relevant equations, theorems, and sections.

5. NUMERICAL RESULTS

5.1. *High Order of Accuracy*

The initial conditions

$$u(x,0) = \begin{pmatrix} 1 + 0.5\cos(8\pi x) \\ 1 + 0.5\cos(8\pi x) \\ \dfrac{1}{\gamma - 1} + \dfrac{1}{2} u_1(x,0) \end{pmatrix} \tag{5.1}$$

with periodic boundary conditions, correspond to the linear advection of a cosine density wave. The velocity and pressure are equal to one and remain constant in time. This test problem is chosen to illustrate the advantage of difference operators with a high order of accuracy. The flow is smooth and therefore solved without local grid adaptation or artificial viscosity. Figure 6 depicts the solutions at $t = 0.3$ obtained for the SHOEC scheme with the sixth- and second-order difference operators given in the appendix,[4] and the first-order Godunov scheme for 50 grid points.

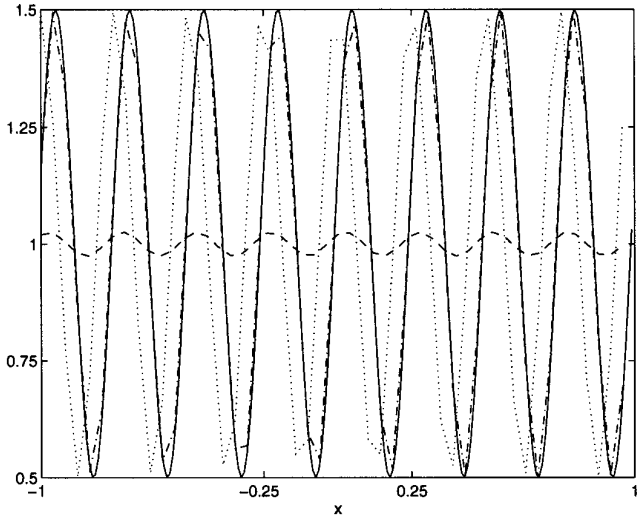

FIG. 6. Solid line exact solution, sixth order (–.), second order (·), first order (—).

To achieve the same accuracy as the sixth-order scheme, a minimum of 250 grid points is needed for the second-order scheme and at least 2000 grid points for the first-order scheme.

5.2. *Shock Detection, Local Grid Adaptation and Artificial Viscosity*

We consider the initial condition

$$u(x,0) = \begin{cases} \begin{pmatrix} 3.857143 \\ 10.141852 \\ 39.166666 \end{pmatrix}, & x < -4, \\ \begin{pmatrix} 1 + 0.2\sin 5x \\ 0 \\ 2.5 \end{pmatrix}, & x \geq -4. \end{cases} \tag{5.2}$$

A *strong* shock wave, moving to the right, interacts with a sine wave of small amplitude. The shock speed $s = 3.55$, resulting in a Mach-number $M \approx 3$ in front of the shock. The difficulty lies in resolving the low and high frequency oscillations that are formed behind the shock wave in the density. This problem is a good test for resolution, as well as the detection algorithm, artificial viscosity, and local grid adaptation. The solution is not known analytically.

[4] Note that because of the periodic boundary conditions the global accuracy is sixth- and second-order respectively as well.

For comparison, an ''exact'' solution is computed using a formally conservative fourth-order central scheme with $n = 2000$ (no grid adaptation) and $t = 1.8$. The artificial viscosity term used is (3.2) with the scalar viscosity ε given by (3.18). The conservative form will ensure that the shock location is correct, which is then used as an extra check for the shock location returned by the SHOEC scheme. In all of the following figures, the shock location is denoted by $*$. The density is shown in Fig. 7a. Again, the computed solution is indicated by a dashed line and the points in the shock are circled. The shock is resolved very sharply which illustrates the effectiveness of the artificial viscosity.

Figures 7b and c show the coarse grid solutions for a fourth-order SHOEC scheme obtained for $n = 400$ and $n = 200$, respectively. The difference operators are given in Appendix B. We used local grid adaptation and one level of refinement (n is the number of coarse grid points). The shock location is determined with the detection algorithm; a priori knowledge of the shock speed is not used. The ratio of fine to coarse grid points is 4. The artificial viscosity is given by (3.3) and (3.18). In Fig. 7d we depict the location of the fine grid relative to the coarse grid as time progresses for $n = 400$. The true and detected shock locations coincide. Clearly, the refined grid is confined to the shock region. Slightly more points are flagged downstream of the shock because of the oscillations. The solution for $n = 400$ is very accurate. For $n = 200$ the peaks are somewhat damped, but the principal features of the flow are clearly visible. In both cases, the shock is resolved very sharply. The detection algorithm and the regridding procedure only accounted for 5% of the total time in these experiments. The effectiveness of our proposed technique is more apparent when we compare our results to those obtained with a fifth-order ENO scheme and third-order limiter as developed by Lindström in [14]. His result for $n = 400$ is shown in 7e. Although this solution is of slightly better quality than ours, the shock resolution is comparable, and the costs of computing our solution are lower than the ENO scheme.

6. CONCLUSIONS

We have presented a high order scheme for the Euler equations that satisfies a semidiscrete energy estimate, as well as an efficient strategy for computing sharp shock solutions. The high order of accuracy of this split high-order entropy conserving (SHOEC) scheme leads to a very efficient scheme for flows that are smooth in large regions of the flow domain. The construction of the SHOEC scheme is based on a symmetrization of the equations, followed by a canonical splitting of the flux vector, and difference operators that satisfy a summation-by-parts principle. The same techniques can be applied to the Navier–Stokes equations, as well as other conservation laws that satisfy conditions mentioned in [20]. We are currently developing a SHOEC scheme for mixed hyperbolic–parabolic equations in ocean modeling.

Although the scheme is in nonconservative form, the shock location obtained in numerical experiments is correct and converges with h. In [24], Salas and Iollo formulated shock jump conditions for the Euler equations in their primitive, nonconservative, form. Jump conditions for the symmetrized split Euler equations are being investigated.

We constructed a cheap and effective scalar artificial viscosity that is used in locally refined grids in the shock region. It results in sharp shock resolution. The positioning of the finer subgrids is aided by a detection algorithm based on a multiscale wavelet analysis of the pressure grid function. The algorithm detects shocks and local oscillations efficiently. No a priori knowledge of the shock location is used and the resulting method is therefore shock capturing. The detection algorithm does not depend on the numerical method and is of general interest. It would be used in, for example, the high-order methods by LeVeque and Shuye [13] that need an accurate shock detector.

The sharp shock resolution and computational efficiency of the above described SHOEC scheme with local grid adaptation are illustrated by the numerical experiments.

The SHOEC scheme, artificial viscosity, and shock detection are generalizable to multiple dimensions. In a forthcoming report we will present numerical results for multidimensional applications in which we use the technique of overlapping grids as well as local grid adaptation. The research presented in this paper is part of a general project to design efficient solution strategies for fluid flows based on stable higher order finite difference methods.

APPENDIX A: SYMMETRIZATION

For $h(S) = e^{S/(\alpha+\gamma)}$,

$$w = \frac{p^*}{p}\begin{bmatrix} E + \dfrac{\alpha-1}{\gamma-1}p & -m & \rho \end{bmatrix}^{\mathrm{T}}$$

and

$$u_w = \frac{1}{p^*}\begin{bmatrix} a\rho & am & \dfrac{a}{2}\rho v^2 - \dfrac{1}{\gamma-1}p \\ & a\rho v^2 - p & v\left(\dfrac{a}{2}\rho v^2 - bp\right) \\ & & -\dfrac{b}{\gamma-1}\dfrac{p^2}{\rho} - bpv^2 + \dfrac{a}{4}\rho v^4 \end{bmatrix}.$$

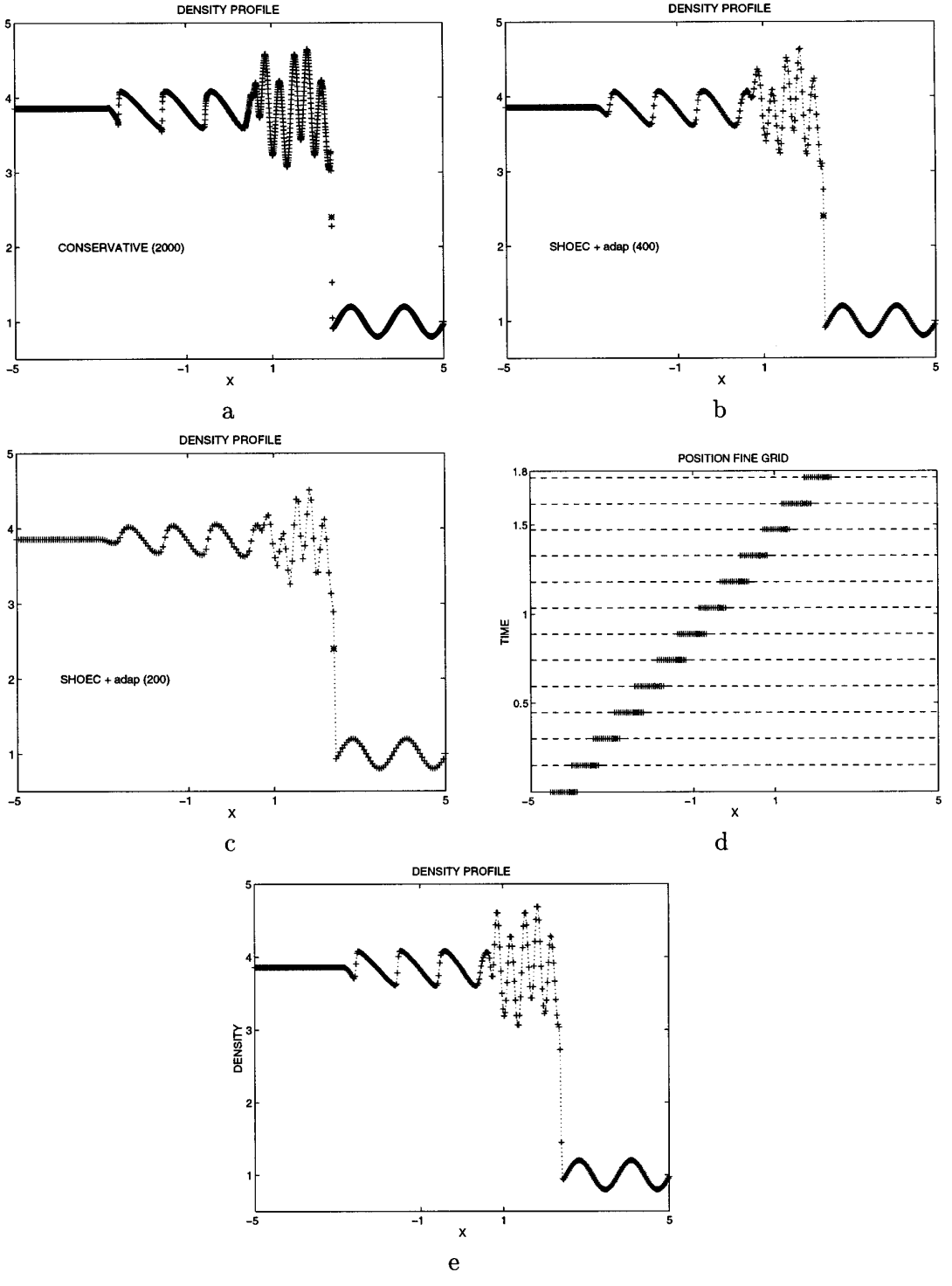

FIG. 7. Density plots for (5.2) at $t = 1.8$ s; exact shock location (∗): (a) reference solution, $n = 2000$; (b) + (c) SHOEC scheme with local grid adaptation: (b) $n = 200$, (c) $n = 400$; (d) position of refined grid, $n = 200$, exacted and detected shock position (∗); (e) fifth-order ENO scheme with third-order limiter; $n = 400$.

Here, p^* and p are related through Eqs. (2.19). The constants a, b, and c are $a = (1 - a - \gamma)/\alpha$, $b = \gamma/(\gamma - 1)$, and $c = (1 - 2\gamma)/(\gamma - 1)$.

The flux vector

$$\tilde{f}(w) = \frac{p}{p^*}\left[-w_2 \quad \frac{w_2^2}{w_3} + p^* \quad -\frac{w_2}{w_3}\left(w_1 + \frac{\gamma - \alpha}{\gamma - 1}p^*\right)\right]^{\mathrm{T}}. \tag{A.1}$$

The upper triangular part of the symmetric matrix $\tilde{f}(w)_w$ expressed in the variables u is given by

$$\tilde{f}_w = \frac{1}{p^*}\begin{bmatrix} am & a\rho v^2 - p & v\left(\frac{a}{2}\rho v^2 - bp\right) \\ & v(a\rho v^2 - 3p) & \frac{a}{2}\rho v^4 - b\frac{p^2}{\rho} - \left(\frac{3}{2} + b\right)pv^2 \\ & & v\left(bc\frac{p^2}{\rho} + cpv^2 + \frac{a}{4}\rho v^4\right) \end{bmatrix},$$

APPENDIX B: DIFFERENCE OPERATORS

We use difference operators that satisfy the summation by parts

$$(\boldsymbol{u}, D\boldsymbol{w})_h = \boldsymbol{u}_n^{\mathrm{T}}\boldsymbol{w}_n - \boldsymbol{u}_0^{\mathrm{T}}\boldsymbol{w}_0 - (D\boldsymbol{u}, \boldsymbol{w})_h, \tag{B.1}$$

for arbitrary discrete grid vectors $\boldsymbol{u}$ and $\boldsymbol{w}$, with respect to the weighted scalar product

$$(\boldsymbol{u}, \boldsymbol{w})_h = h\sum_{i,j=0}^{n}\sigma_{ij}\boldsymbol{u}_i^{\mathrm{T}}\boldsymbol{w}_j. \tag{B.2}$$

The scalar product can also be written as

$$(\boldsymbol{u}, \boldsymbol{w})_h = h\boldsymbol{u}^{\mathrm{T}}\Sigma\,\boldsymbol{w}. \tag{B.3}$$

To establish the semidiscrete estimate for the Euler equations, Σ must be diagonal [22]. In [11], Kreiss and Scherer showed that there exist diagonal Σ and difference operators D of accuracy $2p$ in the interior, $1 \le p \le 4$, such that the summation-by-parts property (B.1) holds. The difference operators D and matrices Σ are computed in [27].

The simplest example is the second-order accurate difference operator

$$D = \frac{1}{h}\begin{bmatrix} -1 & 1 & & & \\ -0.5 & 0 & 0.5 & & \\ & \ddots & \ddots & \ddots & \\ & & -0.5 & 0 & 0.5 \\ & & & -1 & 1 \end{bmatrix},$$

with

$$\Sigma = \begin{bmatrix} 0.5 & & & & \\ & 1 & & & \\ & & \ddots & & \\ & & & 1 & \\ & & & & 0.5 \end{bmatrix}.$$

A sixth-order accurate difference operator D with third-order boundary closure is given by

$$(D\boldsymbol{u})_j = \begin{cases} \frac{1}{h}\sum_{i=0}^{i=8} d_{ji}\boldsymbol{u}_i, & j = 0, ..., 5, \\ \frac{1}{h}\left(-\frac{1}{60}\boldsymbol{u}_{j-3} + \frac{3}{20}\boldsymbol{u}_{j-2} - \frac{3}{4}\boldsymbol{u}_{j-1}\right. & \\ \quad \left. + \frac{3}{4}\boldsymbol{u}_{j+1} - \frac{3}{20}\boldsymbol{u}_{j+2} + \frac{1}{60}\boldsymbol{u}_{j+3}\right), & 5 < j < n - 5, \\ \frac{1}{h}\sum_{i=0}^{i=8} d_{ji}\boldsymbol{u}_{n-i}, & j = n - 5, ..., n. \end{cases}$$

The values of d_{ji}, $0 \le j \le 5$, $0 \le i \le 8$, are given below. The corresponding Σ is diagonal, i.e., $\sigma_{ij} = 0$, $i \ne j$. Its diagonal elements $\sigma_{ii} \equiv \sigma_i$ are

$$\begin{aligned} \sigma_0 &= \sigma_n = 13649/43200 \\ \sigma_1 &= \sigma_{n-1} = 12013/8640 \\ \sigma_2 &= \sigma_{n-2} = 2711/4320 \\ \sigma_3 &= \sigma_{n-3} = 5359/4320 \\ \sigma_4 &= \sigma_{n-4} = 7877/8640 \\ \sigma_5 &= \sigma_{n-5} = 43801/43200 \\ &\vdots \\ \sigma_j &= 1, \quad 5 < j < n - 5, \end{aligned}$$

$d_{00} = -21600/13649$ $d_{01} = 81763/40947$ $d_{02} = 131/27298$
$d_{03} = -9143/13649$ $d_{04} = 20539/81894$ $d_{05} = 0$
$d_{06} = 0$ $d_{07} = 0$ $d_{08} = 0$
$d_{10} = -81763/180195$ $d_{11} = 0$ $d_{12} = 7357/36039$
$d_{13} = 30637/72078$ $d_{14} = -2328/12013$ $d_{15} = 6611/360390$
$d_{16} = 0$ $d_{17} = 0$ $d_{18} = 0$
$d_{20} = -131/54220$ $d_{21} = -7357/16266$ $d_{22} = 0$
$d_{23} = 645/2711$ $d_{24} = 11237/32532$ $d_{25} = -3487/27110$
$d_{26} = 0$ $d_{27} = 0$ $d_{28} = 0$
$d_{30} = 9143/53590$ $d_{31} = -30637/64308$ $d_{32} = -645/5359$
$d_{33} = 0$ $d_{34} = 13733/32154$ $d_{35} = -67/4660$
$d_{36} = 72/5359$ $d_{37} = 0$ $d_{38} = 0$
$d_{40} = -20539/236210$ $d_{41} = 2328/7877$ $d_{42} = -11237/47262$
$d_{43} = -13733/23631$ $d_{44} = 0$ $d_{45} = 89387/118155$
$d_{46} = -1296/7877$ $d_{47} = 144/7877$ $d_{48} = 0$
$d_{50} = 0$ $d_{51} = -6611/262806$ $d_{52} = 3487/43801$
$d_{53} = 1541/87602$ $d_{54} = -89387/131403$ $d_{55} = 0$
$d_{56} = 32400/43801$ $d_{57} = -6480/43801$ $d_{58} = 720/43801.$

See [27] for a derivation of the coefficients.

APPENDIX C: LIPSCHITZ EXPONENT

DEFINITION C.1 (Lipschitz exponent). Let $0 < \alpha < 1$.

1. A function $f(x)$, defined on a domain $D_f \subset \mathbb{R}$, is Lipschitz α over an interval $(x_l, x_r) \subset D_f$, if and only if there exists a constant $C < \infty$ such that for all $x, y \in (x_l, x_r)$

$$|f(x) - f(y)| \leq C|x - y|^{\alpha}.$$

2. A function $f(x)$ is Lipschitz α at a point x_0, if and only if there exists a constant $C < \infty$ such that

$$\sup_{x \in D_f} \frac{|f(x) - f(x_0)|}{|x - x_0|^{\alpha}} \leq C.$$

3. A function that is not Lipschitz 1 at a point x_0 is said to be singular at that point.

4. A distribution is Lipschitz α over an interval (x_l, x_r), if and only if its primitive is Lipschitz $\alpha + 1$ on (x_l, x_r).

5. A distribution $f(x)$ has an isolated singularity Lipschitz α at a point x_0, if and only if $f(x)$ is uniformly Lipschitz α over an interval (x_l, x_r) with $x_0 \in (x_l, x_r)$, and $f(x)$ is Lipschitz 1 over any subinterval of (x_l, x_r) that does not include x_0.

REFERENCES

1. R. Courant and K. O. Friedrichs, *Supersonic Flow and Shock Waves* (Springer-Verlag, New York/Berlin, 1948).
2. I. Daubechies, *Ten Lectures on Wavelets* (SIAM, Philadelphia, 1992).
3. M. Gerritsen, Technical report, SCCM, Stanford University, 1995 (unpublished).
4. M. Gerritsen, Ph.D. thesis, SCCM Program, Stanford University, October 1996 (unpublished).
5. B. Gustafsson and P. Olsson, Technical Report RIACS-94.07, Research Institute of Advanced Computer Science, 1994 (unpublished).
6. A. Harten, Technical Report ICASE 81-34, NASA Langley Research Center, 1981 (unpublished).
7. Ch. Hirsch, *Numerical Computation of Internal and External Flows,* Vol. 2 (Wiley, New York, 1988).
8. T. J. R. Hughes, L. P. Franca, and M. Mallet, *Comput. Methods Appl. Mech. Eng.* **54,** 223 (1986).
9. A. Jameson, Technical Report RIACS 95-16, Research Institute of Advanced Computer Science, 1995 (unpublished).
10. G. Johansson and G. Kreiss, Technical Report TRITA-NA-9219, Department of Numerical Analysis and Computational Science, Royal Institute of Technology Sweden, 1992 (unpublished).
11. H.-O. Kreiss and G. Scherer, Technical report, Department of Scientific Computing, Uppsala University, 1977 (unpublished).
12. R. LeVeque, *Numerical Methods for Conservation Laws,* 2nd ed., (Birkhaeuser, Basel, 1992).
13. R. J. LeVeque and K.-M. Shyue, *SIAM J. Sci. Comput.* **16**(2), 348 (1995).
14. D. Lindström, Ph.D. thesis, Department of Scientific Computing, Uppsala University, June 1996 (unpublished).
15. S. Mallat, *Trans. Am. Math. Soc.* **315,** 69 (1989).
16. S. Mallat and W. L. Hwang, *IEEE Trans. Inform. Theory* **38,** 617 (1992).
17. S. Mallat and S. Zhong, *IEEE Trans. Pattern Anal. Mach. Intell.* **14**(7), 47 (1992).
18. Y. Meyer, *Wavelets and Operators* (Cambridge Univ. Press, Cambridge, 1992).
19. M. S. Mock, *J. Differential Equations* **37,** 70 (1980).
20. P. Olsson. Technical Report RIACS 94-01, Research Institute of Advanced Computer Science, 1994 (unpublished).
21. P. Olsson, *Math. Comput.* **64,** 1035 (1995).
22. P. Olsson. Technical Report RIACS 95-06, Research Institute of Advanced Computer Science, 1995 (unpublished).
23. P. L. Roe, *J. Comput. Phys.* **43,** 357 (1981).
24. M. D. Salas and A. Iollo, Technical Report ICASE 95-12, NASA Langley Research Center, 1995 (unpublished).
25. C.-W. Shu, *SIAM J. Sci. Statist. Comput.* **9**(6), 1073 (1988).
26. B. Sjögreen, private communication.
27. B. Strand, *J. Comput. Phys.* **110**(1), 47 (1994).
28. E. Tadmor, *Math. Comput.* **43,** 353 (1984).
29. X. Zhu and J. Oliger, Technical Report RIACS-94.14, Research Institute of Advanced Computer Science, 1994 (unpublished).